



Localized stress fluctuations drive shear thickening in dense suspensions

Vikram Rathee^{a,b}, Daniel L. Blair^{a,b}, and Jeffrey S. Urbach^{a,b,1}

^aDepartment of Physics, Georgetown University, Washington, DC 20057; and ^bInstitute for Soft Matter Synthesis and Metrology, Georgetown University, Washington, DC 20057

Edited by Morton M. Denn, The City College of New York, New York, NY, and accepted by Editorial Board Member Herbert Levine June 28, 2017 (received for review March 8, 2017)

Dense particulate suspensions exhibit a dramatic increase in average viscosity above a critical, material-dependent shear stress. This thickening changes from continuous to discontinuous as the concentration is increased. Using direct measurements of spatially resolved surface stresses in the continuous thickening regime, we report the existence of clearly defined dynamic localized regions of substantially increased stress that appear intermittently at stresses above the critical stress. With increasing applied stress, these regions occupy an increasing fraction of the system, and the increase accounts quantitatively for the observed shear thickening. The regions represent high-viscosity fluid phases, with a size determined by the distance between the shearing surfaces and a viscosity that is nearly independent of shear rate but that increases rapidly with concentration. Thus, we find that continuous shear thickening arises from increasingly frequent localized discontinuous transitions between distinct fluid phases with widely differing viscosities.

shear thickening | rheology | colloids

The mechanical response of solid particles dispersed in a Newtonian fluid exhibits a wide range of nonlinear phenomena, including a dramatic increase in the viscosity (1–3) with increasing stress, an effect that has important implications for a variety of industrial applications (1, 4) and natural processes (5). If the volume fraction of the solid phase is moderately high, the suspension will undergo continuous shear thickening (CST), where the suspension viscosity increases smoothly with applied shear stress; at still higher volume fractions, the suspension can display discontinuous shear thickening (DST), where the viscosity changes abruptly over several orders of magnitude on increasing applied stress. Proposed models attribute the increase in the bulk viscosity to some form of localized clustering (6, 7) arising from either or both of two distinct types of particle interactions: hydrodynamic (2, 8, 9) and frictional (10–15). However, the physical properties and dynamical behavior of these heterogeneities remain unclear.

Wyart and Cates (W-C) have introduced a phenomenological model, in which the shear thickening arises from a transition from primarily hydrodynamic interactions when the applied stress is substantially below a critical stress, $\sigma \ll \sigma^*$, to primarily frictional interactions when $\sigma \gg \sigma^*$. Although the W-C model and its extensions can reproduce the measured average rheological behavior (7, 12, 13), they do not account for observed temporal fluctuations in bulk viscosity or shear rate (16–18) or local density differences observed in magnetic resonance studies of a cornstarch suspension (19). Similarly, numerical simulations have revealed stress fluctuations at the particle level and larger scales (10, 17). These results indicate that the spatiotemporal dynamics of shear thickening includes complexity that cannot be captured by mean field models, like W-C.

Here, we describe the result of directly measuring the local stresses transmitted to one surface of a sheared suspension using boundary stress microscopy (BSM), a technique that we developed that applies traction force microscopy to rheological experiments (20). We find that the CST regime is characterized by the

appearance of well-defined dynamic localized regions of boundary stresses significantly higher than the applied stress. The spatial extent of these regions is largely determined by the distance between the shearing surfaces, which is two orders of magnitude larger than the size of the particles. The high-stress regions propagate in the shearing direction with an average speed equal to the speed of the fluid halfway between the shearing plates. This behavior is consistent with an intermittent discontinuous transition to a high-viscosity fluid phase. As the applied stress is increased through the shear-thickening region, these high-stress regions become a larger fraction of the total surface area, and the increase accounts quantitatively for the observed shear thickening.

To perform BSM measurements, we replace the bottom rheometer plate with a glass slide coated with a thin, uniform transparent elastomer of known elastic modulus with a sparse coating of chemically bound fluorescent microspheres. We use the measured displacements of the microspheres to determine the stresses at the boundary with high spatial and temporal resolution (*Methods*). We apply BSM to a suspension of silica colloidal particles with radius $a = 0.48 \mu\text{m}$ suspended in an index-matched mixture of glycerol and water. Rheology is performed using a 25-mm cone-plate geometry to ensure a uniform average shear rate, with a fixed, flat-bottom surface and an angled cone that defines the top surface of the sample and rotates in response to the torque applied by the rheometer (Fig. S14).

Bulk Rheology

The rheological response of these suspensions to increasing stress is similar to the typical shear-thickening behavior previously reported (1, 13). Specifically, we observe that the measured

Significance

The nonintuitive behavior of shear-thickening suspensions, such as the familiar cornstarch–water mixture, is a subject of both fundamental and practical importance, but the microscopic phenomena responsible for the dramatic thickening are unknown. Here, we report direct measurements of the stresses at the boundaries of sheared suspensions to reveal dramatic spatial and temporal stress fluctuations not previously reported. We find that the suspension spontaneously and intermittently separates into two different fluid phases with substantially different properties, thus showing that the discontinuous liquid–solid transition that is the most dramatic form of shear thickening is actually ubiquitous and responsible for the observed shear thickening, even in regimes where the average viscosity increases smoothly with applied shear.

Author contributions: V.R., D.L.B., and J.S.U. designed research; V.R. performed research; V.R., D.L.B., and J.S.U. analyzed data; and V.R., D.L.B., and J.S.U. wrote the paper.

The authors declare no conflict of interest.

This article is a PNAS Direct Submission. M.M.D. is a guest editor invited by the Editorial Board.

¹To whom correspondence should be addressed. Email: urbachj@georgetown.edu.

This article contains supporting information online at www.pnas.org/lookup/suppl/doi:10.1073/pnas.1703871114/-DCSupplemental.

viscosity, η , as a function of the applied shear stress, σ , is strongly non-Newtonian for concentrations $\phi = V_p/V > 0.3$, where V_p and V are the total particle volume and the system volume, respectively (Fig. 1A). When $\phi = 0.35$, we observe moderate shear thinning for $\sigma < 10$ Pa followed by a Newtonian plateau and finally, shear thickening, indicated by a small increase in η above an onset or critical shear stress σ_c (Fig. 1A, white circles). For concentrations of $\phi \geq 0.5$, strong thinning is followed by an increase in the plateau viscosity, and above σ_c , η scales with an exponent β ($\eta \propto \sigma^\beta$) that increases with ϕ (Fig. 1A). As previously reported, σ_c does not show significant concentration dependence (7, 13, 21). For this system, we observe discontinuous thickening $\beta = 1$ at $\phi = 0.58$; here, we focus on concentrations below this value.

Although the temporally averaged response provides a bulk picture of CST, the time-resolved rheology reveals substantial fluctuations. Fig. 1B shows the strain rate reported by the rheometer as a function of time for suspensions at $\phi = 0.56$ with a constant applied stress for 180 s. The fluctuations represent variations in the shear rate as the rheometer adjusts the rotation rate of the cone that defines the upper boundary of the suspension to maintain a constant total stress. For stresses below the onset of shear thickening, $\sigma_c \sim 50$ Pa, fluctuations are nearly absent (Fig. S2). We observe that, as the stress is increased above σ_c , the rapid increase in the viscosity is associated with a marked increase in the magnitude of the fluctuations (Fig. 1B). Below $\phi < 0.54$, we do not see any fluctuations in $\dot{\gamma}$ (Fig. S3), although η does increase substantially above σ_c .

BSM

In addition to measuring the system-averaged viscosity vs. time under constant stress, we measure the spatially resolved boundary stresses at specific locations in the rheometer using BSM. The deformations of the elastic substrate arise from the stresses exerted by the suspension at the boundary, $\sigma^b \cdot \hat{n}$, where σ^b is the suspension stress tensor evaluated at the boundary with the substrate, and \hat{n} is the normal to the boundary surface. We report the component of the boundary stress $\sigma^b \cdot \hat{n}$ in the velocity (x direction) represented as σ_x .

Below the onset of shear thickening, the displacements of the elastic substrate and therefore the calculated boundary stresses are spatially and temporally uniform. However, above σ_c and for concentrations $\phi \geq 0.52$, we observe the appearance of localized surface displacements that are much higher than the average displacement.

Fig. 1C shows an example of the spatial map of the component of the boundary stress in the velocity direction calculated from the measured displacement fields. The field of view is $890 \times 890 \mu\text{m}^2$, and the regions of high stresses are large compared with the particle size. Moreover, the total area imaged represents 0.16% of the total surface area of the system, indicating that the spatial scale of the stress variation is much smaller than the scale of the lateral system size (25 mm). Images at higher spatial resolution do not reveal any significant stress variations on smaller length scales down to our instrumental resolution of $\sim 2 \mu\text{m}$ (20).

The regions of high stress at the boundary appear with increasing frequency as the applied stress is increased above σ_c . This increase can be clearly seen in a time series of the average stress in each image (Fig. 1D). At applied stresses just above σ_c , most images do not exhibit high-stress regions and thus, have a small average stress. High-stress fluctuations are clearly separated from the smooth background and appear intermittently separated by large quiescent periods. Even the relatively short regions of low stress evident in the data at $\sigma = 500$ Pa indicate a large number of strain units without high-stress fluctuations, such as can be seen by plotting the average stress vs. strain rather than time (Fig. S4). Significant local stress fluctuations are

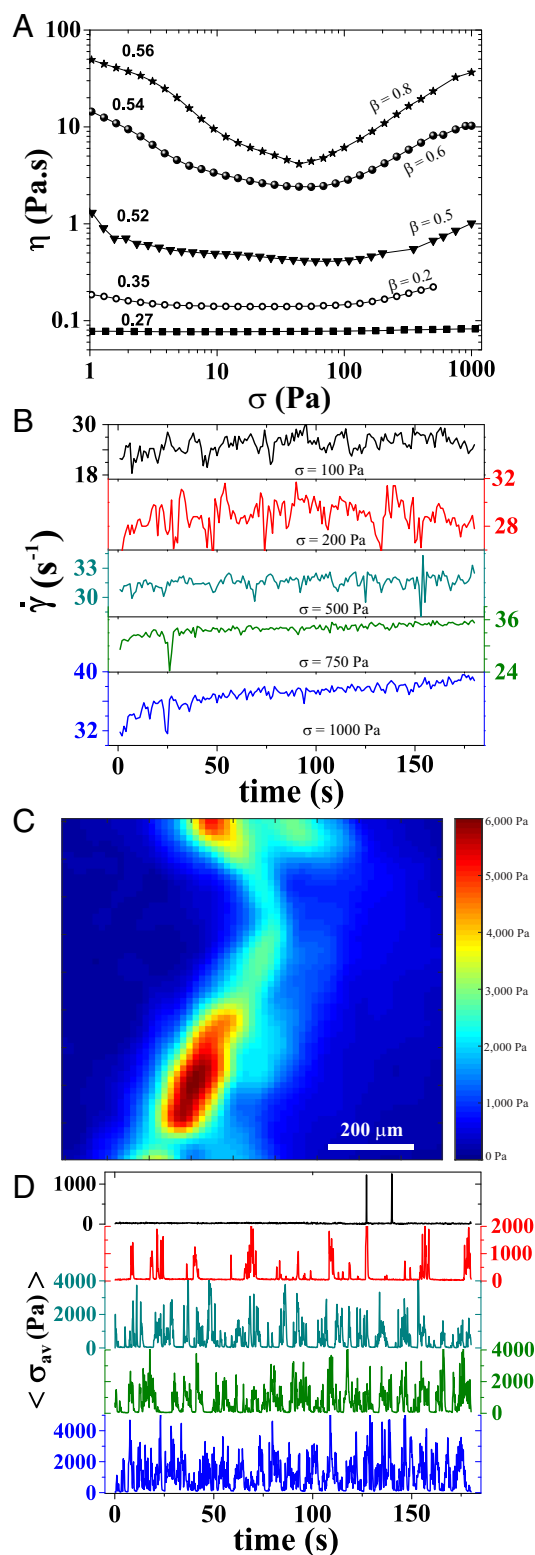


Fig. 1. Rheological and BSM measurements of sheared suspension. (A) Viscosity vs. stress flow curves for suspensions of different concentrations ϕ with the approximate shear-thinning exponent β . (B) Time dependence of the viscosity while shearing at constant applied stress ($\phi = 0.56$). (C) Snapshot of the component of the boundary stress in the velocity direction captured at $\phi = 0.56$ and $\sigma = 1,000$ Pa. (D) Time series of average stress per frame from BSM ($\phi = 0.56$). The same colors refer to the same stress values in B and D.

also observed at $\phi = 0.52$ for applied stresses above σ_c (Fig. S5), although they are both less frequent and smaller in magnitude.

The high-stress regions appear and evolve stochastically, with an overall average translation in the velocity direction (Movies S1–S6). A particularly clear example of that motion is shown as a series of snapshots in Fig. 2A, where a high-stress event that is extended in the vorticity direction moves across the field of view over the course of three frames (representing an elapsed time of $2/7$ s). The average size of the high-stress regions can be assessed from the 2D spatial autocorrelation of the component of the boundary stress in the velocity direction (Methods). Fig. 2B compares the spatial correlation along the velocity direction from BSM measurements taken halfway between the center of the rheometer and the edge, where the gap between the elastic layer and the cone is $h = 100 \mu\text{m}$, with those taken close to the outer edge of the system, where $h = 200 \mu\text{m}$. The autocorrelation curves do not appear to follow a simple functional form, but the comparison suggests that the spatial extent of the high-stress regions in the velocity direction is determined by the rheometer gap. By contrast, the spatial correlation in the vorticity direction does not depend on the gap (Fig. 2B, Inset).

The average motion of the high-stress regions can be quantified by cross-correlating the stress patterns for different time lags (Methods). Fig. 2C shows an example of the temporal cross-correlations along the velocity direction. The decrease in the peak height with time lag is a consequence of the fluctuations as the stress patterns move and disappear erratically, but the displacement of the peaks is indicative of robust propagation in the velocity direction. That propagation velocity scales with the shear rate and is consistently equal to one-half the velocity of the upper boundary at that location in the sample (Fig. 2D), which is the velocity of the suspension at the middle of the $100\text{-}\mu\text{m}$ gap, assuming a symmetric shear profile. These results suggest that the high boundary stresses reflect high-viscosity fluid phases

that span the gap of the rheometer sheared equally from above and below and at rest in a frame comoving with the center of mass of the suspension. We observe qualitatively similar behavior where the gap is $200 \mu\text{m}$; however, the cross-correlations do not show clean peaks, likely because of the higher propagation speed, because the top boundary moves twice as fast as that at the $100\text{-}\mu\text{m}$ gap, and the fact that the size of the high-stress regions is a larger fraction of our field of view. We cannot directly measure the shear profile, leaving open the possibility of a complicated relationship between the dynamics of the high-stress regions and the spatiotemporal dynamics of the suspension rheology.

The appearance of localized boundary stresses with magnitudes that are well above the average stress suggests that the suspension is spontaneously separating into two distinct and coexisting low- and high-viscosity fluid phases during CST, analogous to the low- and high-stress branches of the W-C model but with dynamics that fluctuate in space and time. We can calculate the apparent viscosity of the low-viscosity phase as $\eta_L = \sigma_L / \dot{\gamma}_A$, where σ_L is the average stress in all frames that do not have any high-stress regions, and $\dot{\gamma}_A$ is the average shear rate of the system reported by the rheometer (Methods); η_L shows a modest increase as the applied stress is increased from 100 to 1,000 Pa (Fig. 3A, black squares). We also determine the value of the apparent viscosity of the high-viscosity phase by segmenting the frames showing large stress heterogeneities into low- and high-stress regions using a threshold that is well above the stress generated by the low-viscosity fluid (Methods). The viscosity calculated from the average stress in these regions, $\eta_H = \sigma_H / \dot{\gamma}_A$, is almost two orders of magnitude higher than the low-viscosity fluid and nearly constant over the entire range of applied stress (Fig. 3A, red circles).

The average shear stress exerted by the suspension is the sum of σ_L and σ_H weighted by their respective areas, and therefore,

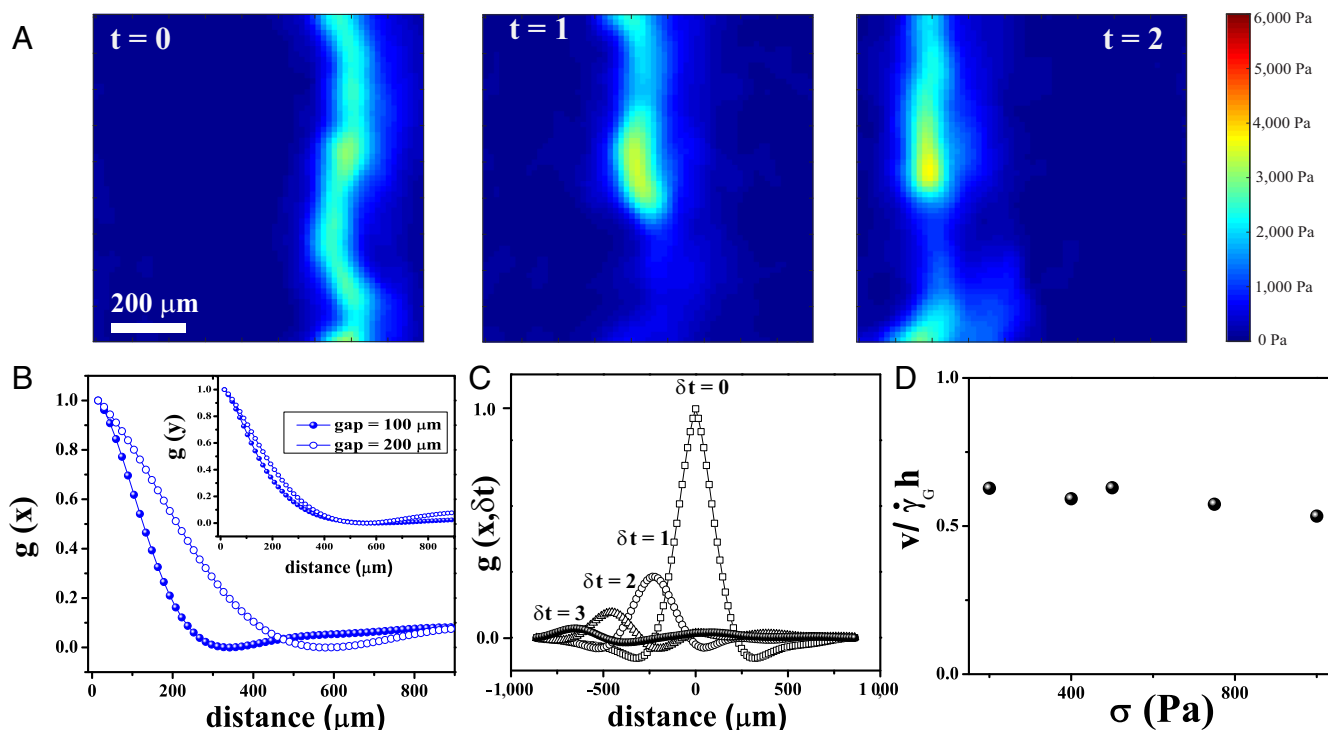


Fig. 2. Correlation analysis using BSM. (A) Snapshots of the stress field at three consecutive time points. (B) Line profiles of $g(x)$, the normalized 2D autocorrelation of $\sigma_x(\vec{r})$, along the velocity direction at two values of the rheometer gap. (Inset) Profiles of $g(y)$, the autocorrelation along the vorticity direction. (C) Evolutions of the average temporal cross-correlation, $g(x, \delta t)$, at different time lags ($\sigma = 1,000 \text{ Pa}$, $h = 100 \mu\text{m}$). (D) Propagation velocity of high-stress regions scaled by the velocity of the top boundary ($h = 100 \mu\text{m}$).

behavior is consistent with the protrusion observed in colloidal as well as granular suspensions on the free surface near the outer open boundary during shear thickening (14). These observations highlight the importance of the boundaries during the transition to DST and the complexity of the spatiotemporal dynamics in this regime.

Discussion

Based on our BSM measurements, the suspension behavior can be divided into three different regimes: (i) $0.3 < \phi < 0.52$, (ii) $0.52 \leq \phi < 0.57$, and (iii) $\phi \geq 0.57$. In regime *I*, the boundary stresses are uniform, and the bulk shear-thickening exponent $\beta < 0.5$. In regime *ii*, propagating regions of high stress appear with a frequency and intensity that increases with applied stress and concentration, and that increase accounts the observed shear thickening. Regime *iii* is characterized by the appearance of very high nonpropagating boundary stresses, indicative of fully jammed regions.

The high-stress regions in regime *ii* show nearly Newtonian apparent viscosities η_H , although it is important to note that η_H , like the average viscosity reported from macroscopic rheology, is calculated from average quantities. If, for example, the shear rate within the high-viscosity phase is highly nonuniform in the gradient direction, η_H would not characterize a true local viscosity. Nonetheless, the behavior in regime *ii*, where regions of the suspension transition abruptly to a high-viscosity phase, is reminiscent of the bifurcation between low- and high-viscosity branches described in the W-C model, representing states with different fractions of frictional contacts created when the stress between particles exceeds the critical stress necessary to overcome the repulsive forces that stabilize the suspension. Because the value of ϕ at which the viscosity diverges depends on the fraction of frictional contacts, an instability arises in certain regimes because of positive feedback between the increased local stress and viscosity resulting from the added frictional contacts between particles. Our results are consistent with a model where the high-stress state appears intermittently in localized clusters with a size determined by the rheometer gap, a mesoscopic length scale two orders of magnitude larger than the particle scale (Fig. 2*B*). In the W-C model, the instability is present only over a narrow range of concentrations very close to $\phi = 0.58$, and the continuous shear-thickening regime is characterized by a smooth increase in the fraction of frictional contacts as the applied stress increases. Our results imply that the fraction of frictional contacts is spatially heterogeneous and dynamically fluctuating throughout the shear-thickening regime, perhaps because of instabilities that disrupt the formation of stable interfaces between the high- and low-stress branches (18).

The complex stress dynamics revealed by BSM are reminiscent of the large fluctuations in average stress observed in constant shear rate experiments (16), but in our case, they do not generate dramatic temporal variations in the average rheological properties. This difference is likely caused by the feedback present in constant stress experiments: an increase in stress created by a localized transition to the high-viscosity branch will produce a small decrease in shear rate, which in turn, would limit the probability of growth of the high-viscosity region, suppressing system-wide fluctuations. Thus, the feedback mechanism can be different in stress- and strain-controlled measurements (22). A recent investigation of local stress dynamics in granular suspensions in DST using a novel pressure sensitive dye did not reveal stress heterogeneities, but a direct comparison with our results is difficult because of the differences in both the measurement technique and the suspension properties (23). Local fluctuations of stress at the scale of small groups of particles have been observed in computer simulations (10, 17), but the mesoscopic scale apparent from BSM is not present, possibly because of the relatively

small size of the systems simulated or sensitivity to aspects of the particle interactions or suspension hydrodynamics present in the experimental system that are not included in the computational models. Elucidating these issues will require the broad application of BSM to particulate systems and the extension of the technique to measure larger spatial scales. Furthermore, an extension of the theoretical models to include spatial and temporal variations in the relevant structural and mechanical fields will be necessary to determine the physical mechanisms responsible for origin and evolution of the localized regions of a distinct high-viscosity fluid that we have found underlie CST.

Methods

Elastic substrates were deposited on glass cover slides of diameters of 43 mm by spin coating PDMS (Sylgard 184; Dow Corning) and a curing agent. The PDMS and curing agent were mixed at a ratio of 35:1 and degassed until there were no visible air bubbles. Films of thickness of 35 μm were created using spin coating on cover slides of diameter 40 mm (Fisher Sci), cleaned thoroughly by plasma cleaning and rinsing with ethanol and deionized water. After deposition of PDMS, the slides were cured at 85 °C for 45 min. After curing, the PDMS was functionalized with 3-aminopropyl triethoxysilane (Fisher Sci) using vapor deposition for ~ 40 min. For imaging, carboxylate-modified fluorescent spherical beads of radius 0.52 μm with excitation/emission at 480/520 nm were attached to the PDMS surface. Before attaching the beads to functionalized PDMS, the beads were suspended in a solution containing 3.8 mg/mL sodium tetraborate, 5 mg/mL boric acid, and 0.1 mg/mL 1-ethyl-3-(3-dimethylaminopropyl) carbodiimide (Sigma-Aldrich). The concentration of beads used was 0.006% solids.

Suspensions were formulated with silica spheres of radius $a = 0.48$ μm (Bangs Laboratories, Inc.) suspended in a glycerol water mixture (0.8 glycerol mass fraction). The volume fraction is calculated from the mass determined by drying the colloids in an oven at 100 °C.

Rheological measurements were performed on a stress-controlled rheometer (Anton Paar MCR 301) mounted on an inverted confocal (Leica SP5) microscope (24) using a 25-mm diameter cone with a 1° angle. A 10 \times objective was used for imaging and produced a 890 \times 890 μm^2 field of view (Fig. S1). Images were collected at a rate of 7 frames s^{-1} . Deformation fields were determined with particle image velocimetry (PIV) in ImageJ (25). For some experiments, fluorescent beads with excitation/emission at 480/520 nm were added to the silica suspension as tracer particles at a ratio of 1:100. In that case, we have attached beads with different excitation/emission spectra (660/680 nm) on the PDMS, used 480/520-nm tracer beads, and imaged the system with two separate laser lines. The surface stresses at the interface are calculated using an extended traction force technique and codes given in ref. 26. In all cases, the reported stresses are the component of the boundary stress in the velocity (x direction) and represented as σ_x . Measurement noise arises primarily from the resolution of the PIV technique. For the PDMS stiffness used, we observe apparent stress fluctuations of ± 10 Pa in σ_x around the mean value. Normalized 2D spatial autocorrelations $g(\delta\vec{r}) = \langle \delta\sigma_x(\vec{r}, t) \delta\sigma_x(\vec{r} + \delta\vec{r}, t) \rangle / \langle \delta\sigma_x(\vec{r}, t)^2 \rangle$, averaged over \vec{r} and t , are calculated using the Matlab function `xcorr2`. Temporal cross-correlations, $g(\delta\vec{r}, \delta t) = \langle \delta\sigma_x(\vec{r}, t) \delta\sigma_x(\vec{r} + \delta\vec{r}, t + \delta t) \rangle / \langle \delta\sigma_x(\vec{r}, t)^2 \rangle$, are calculated similarly. The profile of the spatial autocorrelation along the velocity direction, $g(x)$, is calculated from $g(\delta\vec{r})$ by setting $y = 0$, whereas setting $x = 0$ gives the profile along the vorticity direction, $g(y)$. Similarly, the temporal cross-correlation in the velocity direction, $g(x, \delta t)$, is calculated from $g(\delta\vec{r}, \delta t)$ by setting $y = 0$.

The average stress in the high-stress regions is calculated as

$$\sigma_H = \langle \sigma_x(\vec{r}_i) \rangle, \quad [2]$$

where the average is taken only over the positions \vec{r}_i that satisfy the condition that $\sigma_x(\vec{r}_i) > 500$ Pa as indicated by the circles in Fig. S7*D*. Fig. S7 shows how the regions identified as high stress evolve as the threshold is changed. The absolute values of σ_H are only weakly dependent on the threshold for the value used here. The average stress produced by the low-stress phase is calculated by averaging $\sigma_x(\vec{r}_i)$ from those images where the stress value at every position satisfies the condition $\sigma_x(\vec{r}_i) < 500$ Pa.

ACKNOWLEDGMENTS. We thank Emanuela Del Gado, David Egolf, Peter Olmsted, and John Royer for helpful discussions, and Eleni Degaga and Jim Wu for their contributions to protocol development. This work was supported by Air Force Office of Scientific Research Grant FA9550-14-1-0171. D.L.B. is supported, in part, by Templeton Foundation Grant 57392. J.S.U. is supported, in part, by the Georgetown Interdisciplinary Chair in Science Fund.

Supporting Information

Rathee et al. 10.1073/pnas.1703871114

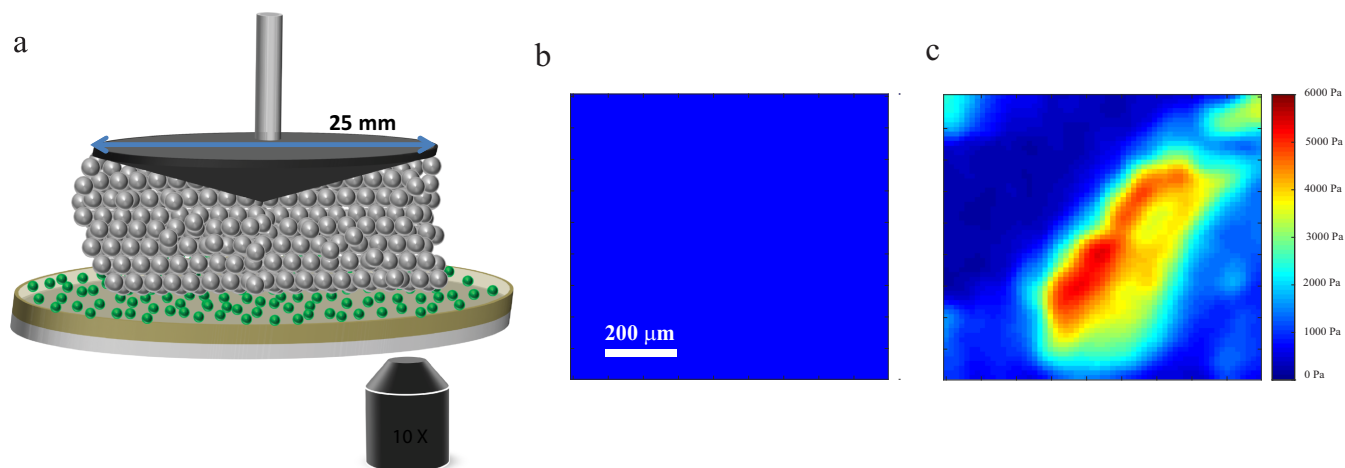


Fig. S1. (A) Schematic of the BSM setup. The bottom cover slide of thickness 100 μm is shown in silver, and the 35- μm PDMS layer is shown in light green. Fluorescent microspheres attached to the PDMS are shown in green. The silica colloids are shown in silver. The rheometer cone defines the top surface of the suspension and is attached to a stress-controlled rheometer. The calculated stress field is shown for representative (B) uniform ($\sigma = 500$ Pa at $\phi = 0.50$) and (C) heterogeneous ($\sigma = 1,000$ Pa at $\phi = 0.56$) cases.

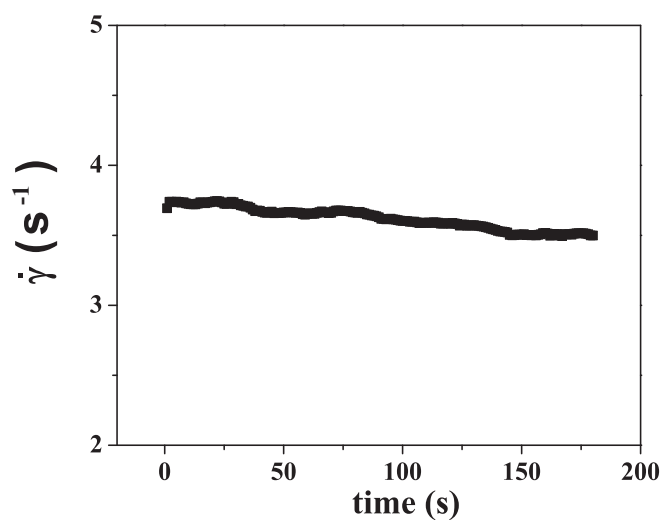


Fig. S2. Time-dependent viscosity (η) at a constant applied stress $\sigma = 10$ Pa (below critical stress) at $\phi = 0.56$.

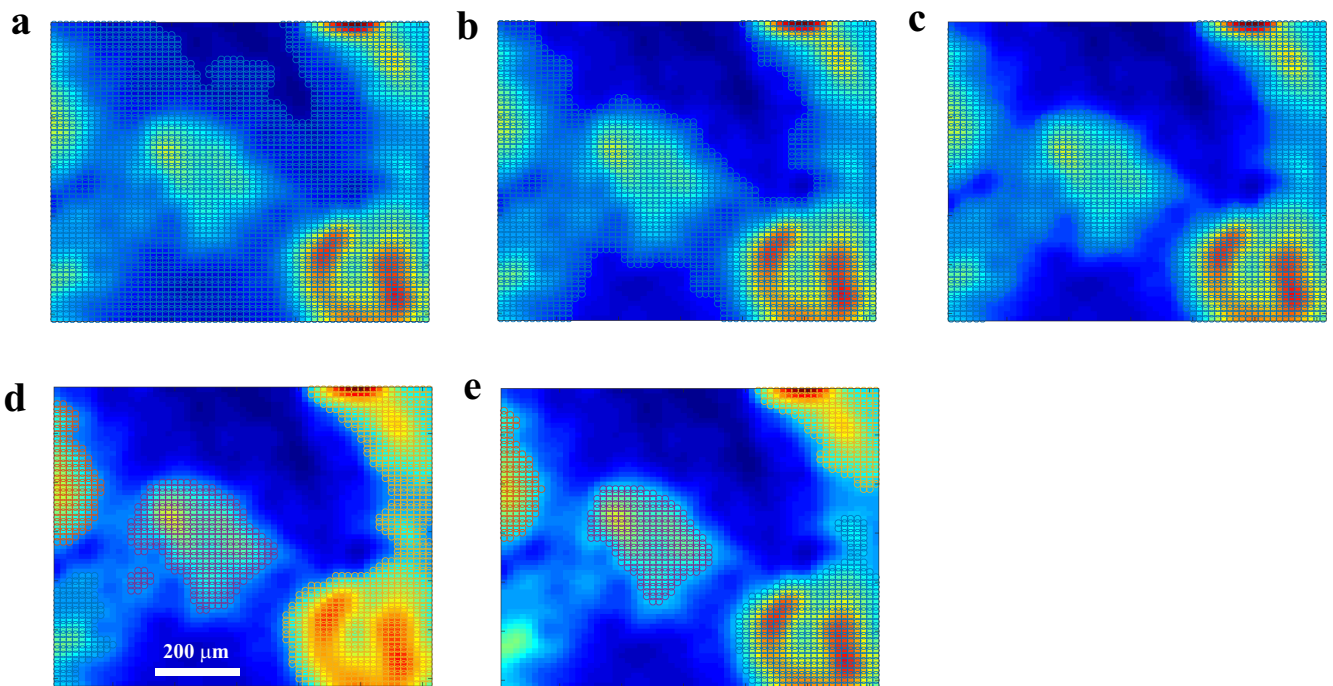
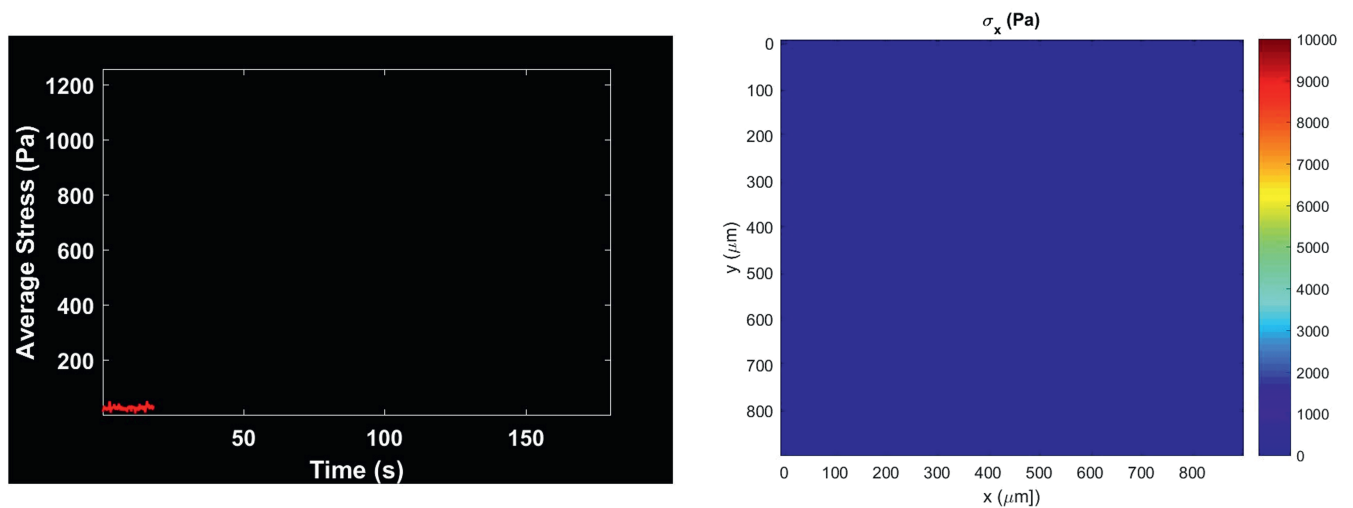
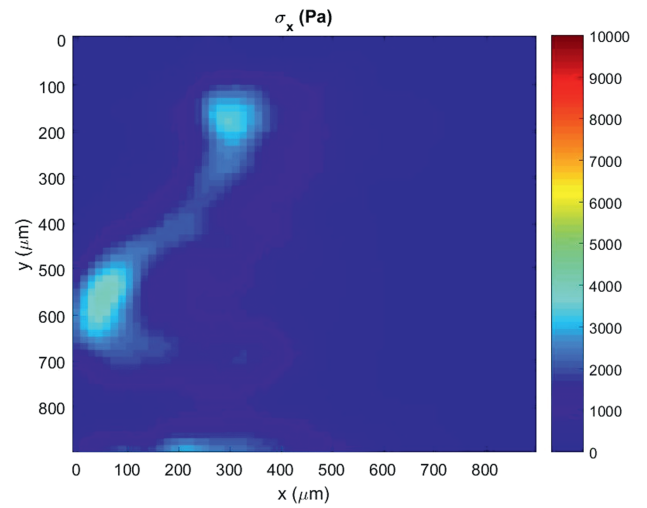
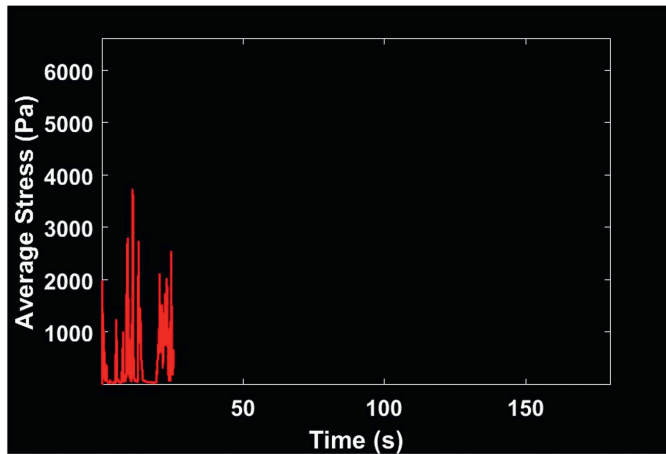


Fig. S7. Identification of high-stress regions for different threshold values. The circles mark regions above threshold for values (A) 100, (B) 250, (C) 400, (D) 500, and (E) 600 Pa (gap = 100 μm , $\sigma = 1,000$ Pa).



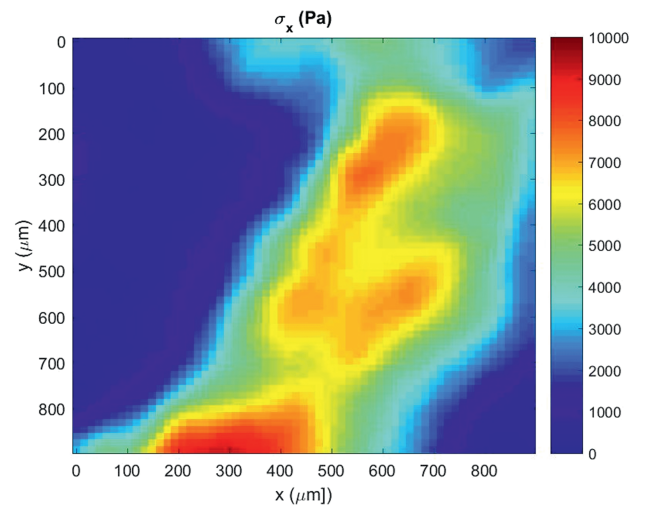
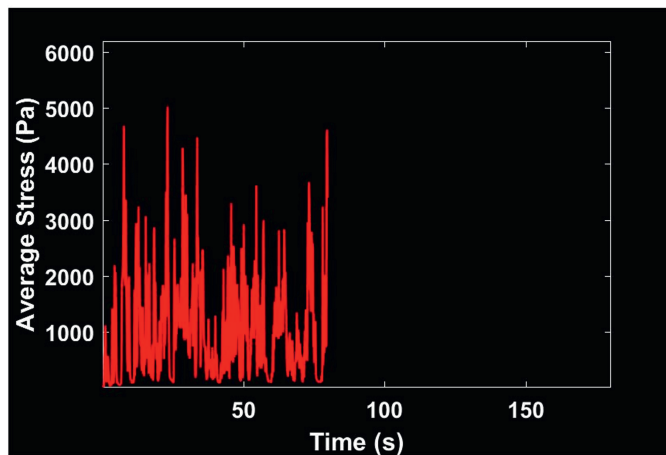
Movie S1. Time evolution of average stress calculated from (Left) BSM and (Right) dynamic stress map at $\phi = 0.56$, $\sigma = 100$ Pa, and gap = 200 μm . Total elapsed time is 180 s, and average $\dot{\gamma} = 24.75 \text{ s}^{-1}$.

[Movie S1](#)



Movie S2. Time evolution of average stress calculated from (Left) BSM and (Right) dynamic stress map at $\phi=0.56$, $\sigma=500$ Pa, and gap= 200 μm . Total elapsed time is 180 s, and average $\dot{\gamma}=31.05$ s^{-1} .

[Movie S2](#)



Movie S3. Time evolution of average stress calculated from (Left) BSM and (Right) dynamic stress map at $\phi=0.56$, $\sigma=1,000$ Pa, and gap= 200 μm . Total elapsed time is 180 s, and average $\dot{\gamma}=37$ s^{-1} .

[Movie S3](#)

